WILEY-VCH

Supporting Information

Dual-site Hydrogen Bonding in 3D Hybrid Halide Perovskitoid Towards Stable and Sensitive Ultraviolet Light Detection

Yao Li,[a] Hang Li,[a] Qianwen Guan,[a] Huang Ye,[a] Chengshu Zhang,[a] Lijun Xu,[a] Haiqing Zhong,[a] Xinwei Zhou,[a] Junhua Luo*[a]

a State Key Laboratory of Functional Crystals and Devices, Fujian Institute of Research on the Structure of Matter, Chinese Academy of Sciences, Fuzhou, Fujian 350002, China

b University of Chinese Academy of Sciences, Beijing 100049, China

c School of Physical Science and Technology, ShanghaiTech University, Shanghai 201210, China

d Fujian College, University of Chinese Academy of Sciences, Fuzhou 350000, China

E-mail: jhluo@fjirsm.ac.cn

Experimental Section

Chemicals. N-methylpropane-1,3-diamine (3-MAPA, Picasso, 99.79%), lead (II) acetate trihydrate ($Pb(Ac)_2{\cdot}3H_2O$, Aladdin, 99.5%), hydriodic acid (HI, Adamas, 55-57%), hypophoaphoeous acid ($H_4O_4P_2$, Rhawn, 50%). All the chemicals were bought and used without further purification.

Synthesis and Crystal Growth. To synthesise high quality (3-MAPA)Pb_2I_6 single crystals, the composition and temperature of the solution must be precisely controlled. 3-MAPA (5 mmol; 0.44 g), and $Pb(Ac)_2{\cdot}3H_2O$ (10 mmol; 3.793g) were dissolved in hydriodic acid solution (55%, 15 mL) to which the hypophoaphoeous acid solution (50%, 1 mL) was added, heated at 80°C and stirred until a yellow and transparent solution formed, until well mixed. The solution was then gradually cooled at an initial temperature of 80°C at a rate of 1°C per day until 30°C. This slow cooling promotes controlled nucleation and growth, resulting in the formation of high-quality, centimetre-sized (3-MAPA)Pb_2I_6 red single crystals.

Powder X-ray diffractions (PXRD) determination. PXRD was performed on the MiniFlex 600 X-ray diffractometer equipped with Cu K_α radiation. The diffraction patterns were collected in the 2θ range of 5°-50° with a step size of 0.02°.

Single Crystal X-ray Diffraction. Crystallographic data for (3-MAPA)Pb_2I_6 at 273K were collected using a Synergy-R single crystal diffractometer with Mo-Kα radiation (λ = 0.71073 Å). Crystal structures were determined using direct methods and refined using the full-matrix least-squares method based on F2 with the SHELXLTL 2018 package. Hydrogen atoms in organic cations were refined geometrically, while non-hydrogen atoms were refined isotropically. Detailed crystallographic data and refinement parameters at room temperature are provided in Table S1.

Molecular Interaction Analysis. The interlayer interactions in MPI structure are analyzed using the CrystalExplorer program.

Morphology Characterization. Atomic force microscopy (AFM) and scanning electron microscopy (SEM) images of the surface of MPI single crystals were obtained using a Bruker Dimension Icon AFM and a JEOL JSM-6700F field emission SEM, respectively.

Density Functional Theory (DFT) Calculation. First-principles density function theory (DFT) calculations were performed with the Cambridge Sequential Total Energy Package (CASTEP). The exchange-correlation functional was described by a generalized gradient approximation (GGA) with the revised Perdew-Burke-Ernzerhof functional for solids (PBEsol) scheme. The interactions between the ionic cores and the electrons were described by the norm-conserving pseudopotential. The numbers of plane waves included in the basis sets were determined by a cutoff energy 820 eV. To achieve the accurate density of the electronic states, the k-space integrations were done with Monkhorst-Pack grids with a 6 × 6 × 3 k-point. In the optical property calculations, the dense grid of 3 × 6 × 6 k-points and more than 100 empty bands are adopted to guarantee the accuracy. The other parameters and convergent criteria were the default values of CASTEP code. The calculations of band structure, density of states, frontier orbitals diagrams were performed using ab initio first-principles density functional theory method within the total-energy code CASTEP program. The effective mass (m*) of carriers existing around the bottom of the conduction band or the top of the valence band was calculated as a result of the fitting of the dispersion relation using the formula of

$$\frac{1}{m^*} = \frac{1}{\hbar}\frac{\partial E(k)}{\partial k^2}$$

where $\hbar$ is the reduced Planck constant, E(k) is the electron energy at the wave vector k in the energy band.

Optical property and photoconductivity measurements. At room temperature, the solid-state ultraviolet absorption spectrum of MPI was measured using a PerkinElmer Lambda 950 UV-Visible spectrophotometer. Photovoltaic measurements were conducted on a two-terminal device fabricated from MPI under 377 nm laser illumination.

Structural and optoelectronic analysis.

The distortion index (Δd) of inorganic skeleton is calculated from the formula $\Delta d = \frac{1}{6}\sum\left[\frac{d_n - d}{d}\right]^2$, where d_n reference Pb-I bond length and d refer to the average value of the Pb-I bond length.

The bond angle variance σ^2 is calculated from the formula $\sigma^2 = \sum_{i=1}^{12}\frac{(\theta_i - 90)^2}{11}$, where θ_i refer to the I-Pb-I bond angle. Responsivity (R) and detectivity (D*) can be calculated from the formula $R = \frac{J_{in}}{P_{in}}$ and $D^* = \frac{J_{in}}{P_{in} \times 2eJ_{dark}}$, where J_{in}, P_{in}, e, and J_{dark} represent current density, incident light power density, elementary charge, and dark current density, respectively.

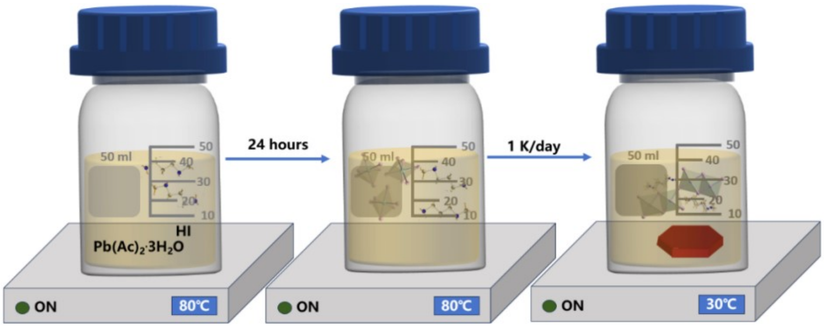

Figure S1. Schematic representation of the growth process of MPI.

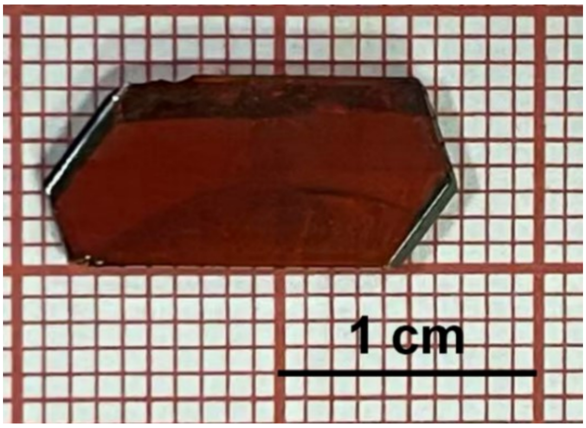

Figure S2. The photograph of high-quality MPI bulk single crystal.

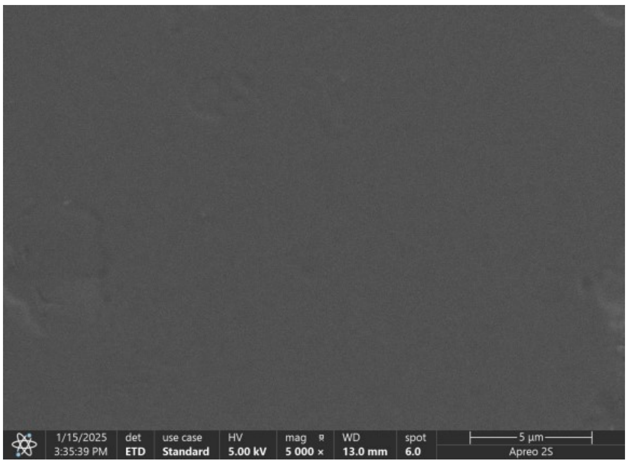

Figure S3. SEM image of the (0k0) crystallographic planes of MPI.

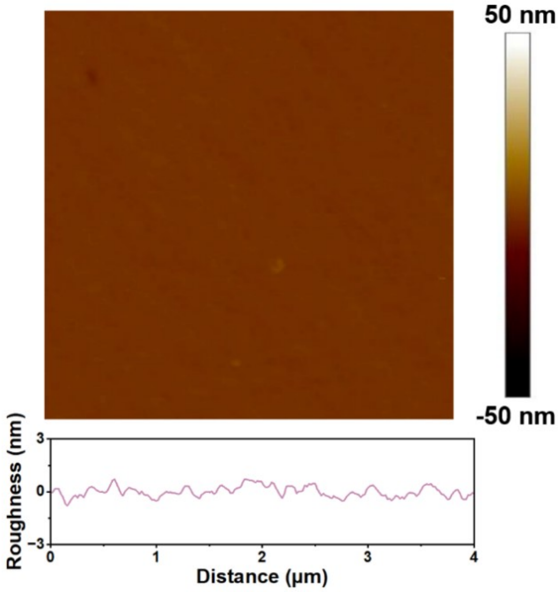

Figure S4. AFM image of the (0k0) crystallographic planes of MPI.

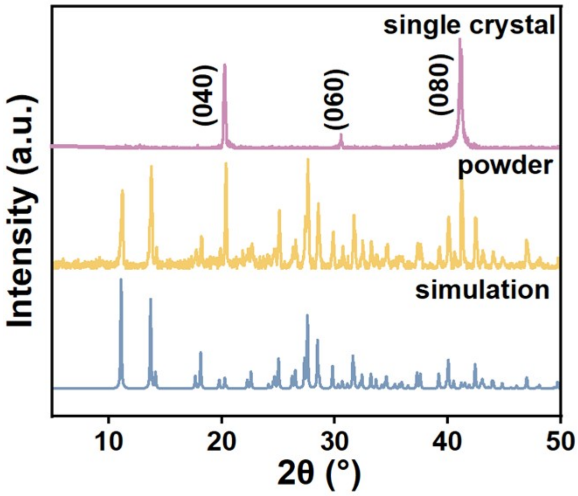

Figure S5. The simulated, experimental powder and bulk single crystal XRD patterns of MPI.

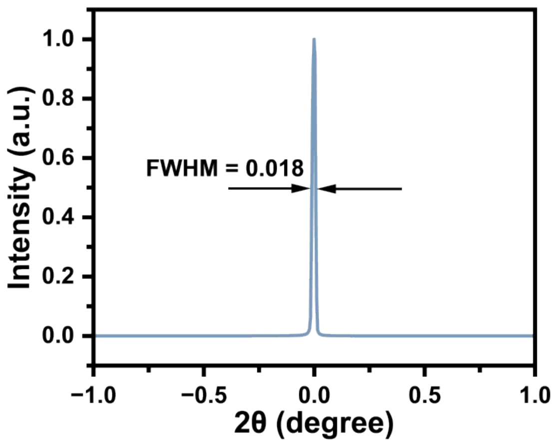

Figure S6. The corresponding image of high-resolution XRD rocking curves of the (080) diffraction peaks.

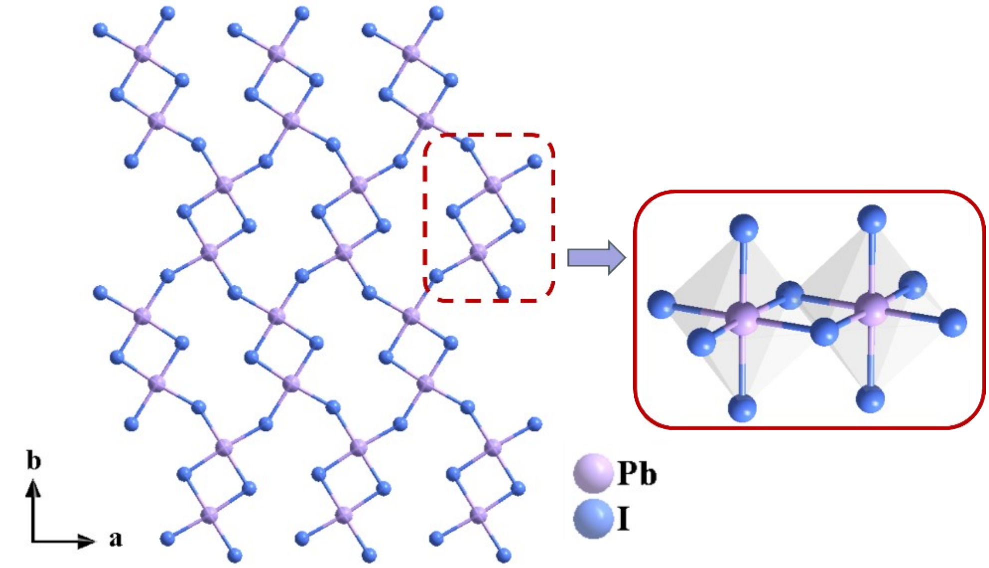

Figure S7. Expanded inorganic skeleton of MPI and $Pb_2I_{10}^{6-}$ dimer.

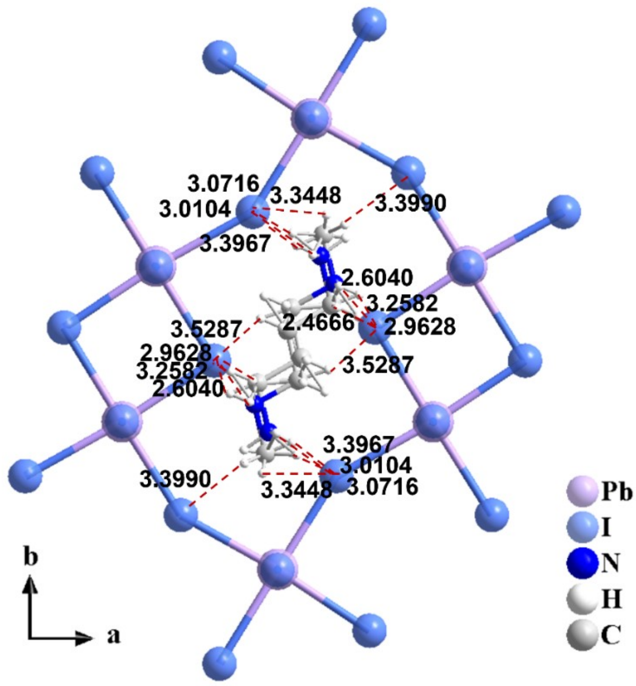

Figure S8. Distances between the halogen iodine and the H atoms on the 3-MAPA^{2+} cation.

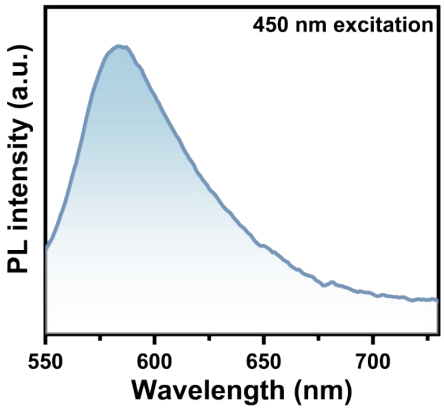

Figure S9. The photoluminescence (PL) spectrum of the MPI

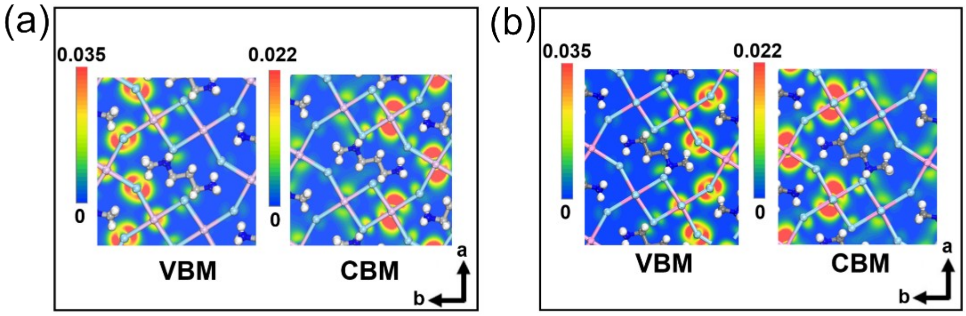

Figure S10. The calculated partial charge density of the VBM and CBM for the two molecular conformations of MPI along the ab-plane.

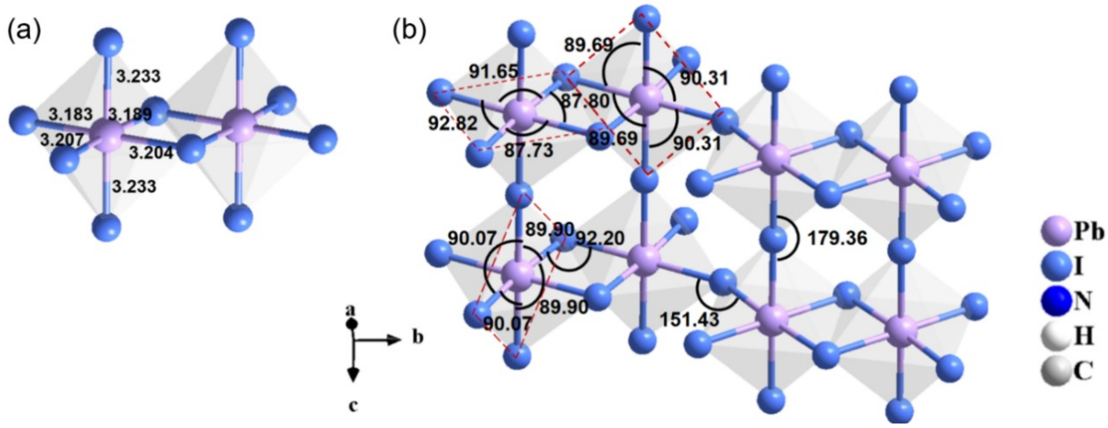

Figure S11. The crystal structure shows detailed bond length (a) and bond angles (b) in MPI.

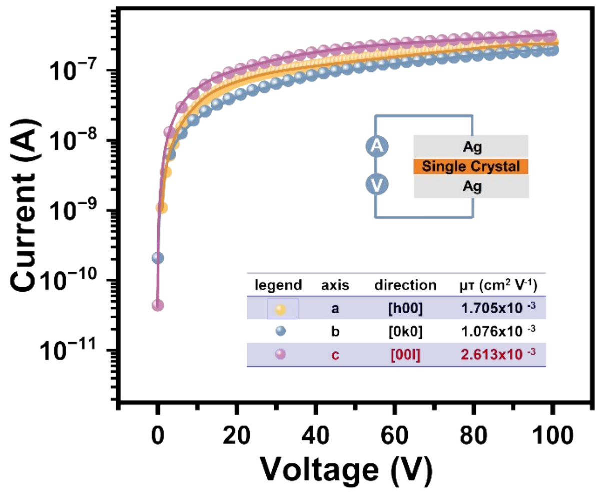

Figure S12. The direction-dependent carrier mobility-lifetime ($\mu\tau$) product of MPI.

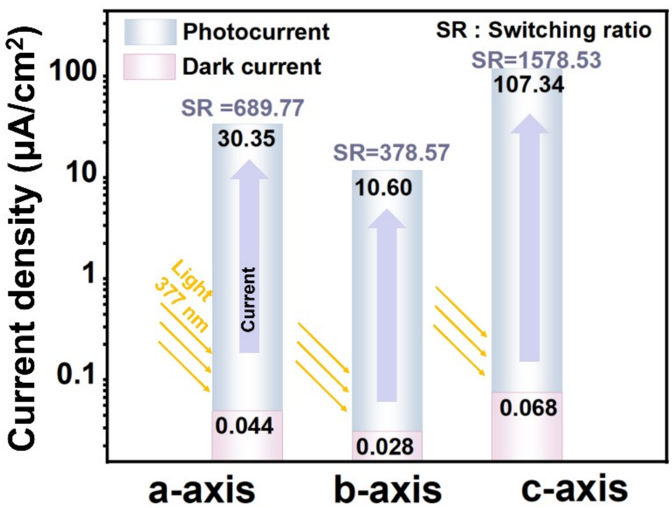

Figure S13. Comparison of the dark current, photocurrent (4.965 mW cm^{-2}), and switching ratio of MPI along the crystallographic a, b, and c-axes under 377 nm illumination.

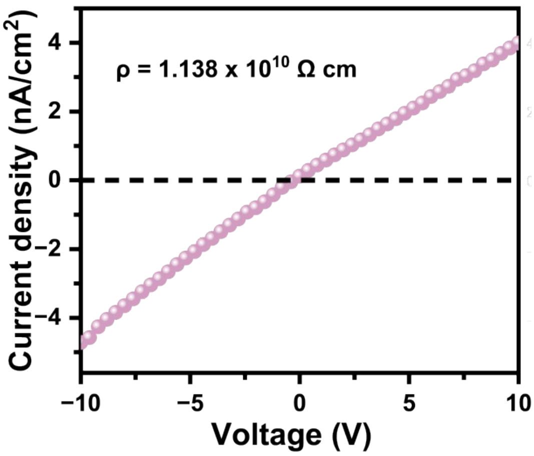

Figure S14. The resistivity of MPI SC.

Table S1. Crystal data and structure refinement for (3-MAPA)Pb_2I_6.

Identification code	(3-MAPA)Pb_2I_6
Empirical formula	$C_4H_{14}I_6N_2Pb_2$
Formula weight	1265.95
Temperature/K	273.15
Crystal system	orthorhombic
Space group	*Pbam*
a/Å	8.9786(7)
b/Å	17.5359(13)
c/Å	6.4660(5)
α/°	90
β/°	90
γ/°	90
Volume/Å^3	1018.06(13)
Z	2
ρ_{calc} g/cm^3	4.130
μ/mm^{-1}	25.593
F(000)	1068.0
Radiation	MoKα (λ = 0.71073)
2Θ range for data collection/°	4.646 to 62.094
Index ranges	$-10 \le h \le 13$, $-19 \le k \le 25$, $-9 \le l \le 8$
Reflections collected	8887
Independent reflections	1755 [R_{int} = 0.0686, R_{sigma} = 0.0486]
Data/restraints/parameters	1755/78/81
Goodness-of-fit on F^2	1.065
Final R indexes [I>=2σ (I)]	R_1 = 0.0692, wR_2 = 0.1802
Final R indexes [all data]	R_1 = 0.0799, wR_2 = 0.1976
Largest diff. peak/hole / e Å^{-3}	1.98/-2.222

Table S2. Comparison of some (A)Pb_2I_6-type 3D perovskite with H···I interaction force.

Materials	Space group	H···I	ref
(3-MAPA)Pb_2I_6 (MPI)	Pbam	95.0%	This work
(H_2pda)Pb_2I_6 (2)	P2$_1$/c	93.7%	[1]
(M_2pda)Pb_2I_6 (3)	Pba2	86.7%	
(4AMPY)Pb_2I_6	Ia	82.9%	[2]
(3AMPY)Pb_2I_6	Im	81.9%	
(R/S-3AEP)Pb_2I_6	C222$_1$	82.2%	[3]
(R/S-2AEP)Pb_2I_6	C222$_1$	78.1%	

Table S3. The bond lengths and calculate distortion of the inorganic framework for MPI, 2 and 3.

	$(3\text{-MAPA})Pb_2I_6$ (MPI)	$(H_2pda)Pb_2I_6$ (2)	$(M_2pda)Pb_2I_6$ (3)
	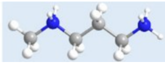	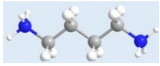	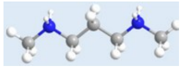
CCDC	2486626	2183780	2183781
Bond length (Å)	3.233	3.190	3.221
Pb-I	3.183	3.122	3.180
	3.207	3.182	3.346
	3.204	3.236	3.090
	3.189	3.309	3.275
	3.233	3.201	3.242
Distortion index (D)	0.00516	0.01369	0.01922

Table S4. The bond angles and calculate bond angles variance of the inorganic framework for **MPI**, **2** and **3**.

	MPI	2	3
Bond anle(°)	87.80	87.66	92.33
I-Pb-I	89.90	87.10	89.32
	89.69	89.52	85.63
	89.69	96.44	93.18
	89.90	90.12	93.27
	87.72	90.46	86.72
	91.65	87.19	90.53
	90.31	95.82	86.00
	90.31	85.04	91.39
	90.07	91.37	90.08
	90.07	90.67	92.20
	92.82	88.94	88.85
The bond angles variance $(\sigma^2)/(deg^2)$	1.92167	11.42371	7.35572

Table S5. The carrier mobility-lifetime ($\mu\tau$) product and dark-current drift comparison of MPI with other perovskite SC detectors.

Material	$\mu\tau$ (cm^2V^{-1})	Dark current drift ($nA\ cm^{-1}\ s^{-1}\ V^{-1}$)	Applied electric (V)	Ref.
$(3\text{-MAPA})Pb_2I_6$	2.61×10^{-3}	8.184×10^{-8}	10	This work
$CsPbI_3$	3.63×10^{-3}	---	200	[4]
$CsPbBr_3$	5.14×10^{-3}	---	5	[5]
$MhyPbBr_3$	1.1×10^{-3}	5.77×10^{-5}	100	[6]
$(S\text{-BPEA})EA_6Pb_4Cl_{15}$	1.0×10^{-4}	---	100	[7]
$(NPA)_2(EA)_2Pb_3Br_{10}$	2.04×10^{-3}	---	0	[8]
$FA_{0.5}MA_{0.5}PbI_3$	4.7×10^{-4}	5.77×10^{-4}	10	[9]
$FA_{0.55}MA_{0.45}PbI_3$	2.91×10^{-3}	---	5	[10]
$(2IPA)_2FAPb_2I_7$	1.20×10^{-3}	7.76×10^{-6}	10	[11]
$(F\text{-PEA})_2PbI_4$	5.1×10^{-4}	4.9×10^{-8}	133 Vmm^{-1}	[12]
$BDAPbI_4$	4.43×10^{-4}	6.06×10^{-9}	10	[13]
$MAPbBr_3$	---	1.2×10^{-3}	20	[14]
$CsPbBr_3$	8.77×10^{-4}	1.9×10^{-4}	---	[15]
$(3\text{-MNPA})PbBr_4$	3.43×10^{-3}	---	0	[16]
$(3AP)PbI_4$	2.38×10^{-3}	---	10	[17]
$(3AP)PbCl_4$	2.74×10^{-3}	---	10	
$MAPbI_3$	---	1.4×10^{-4}	100	[18]
$Cs_3Bi_2I_9$	7.97×10^{-4}	---	10	[19]
$(R\text{-MPz})_6Bi_3I_{21}\cdot6H_2O$	3.24×10^{-4}	---	0	[20]
$MA_3Bi_2I_9$ SC	1.2×10^{-3}	---	20	[21]
$(R\text{-PPA})_2BiI_5$	5.6×10^{-5}	1.40×10^{-4}	10	[22]
$FA_3Bi_2I_9$	2.4×10^{-5}	---	180	[23]

Table S6. Responsivity and detectivity of representative perovskite single-crystal photodetector.

Materials	**Dimensionality**	**Wavelength** (nm)	**Responsivity** (R)	**Detectivity** (D*/Jones)	**Condition (V)**	**Ref.**
$(3\text{-MAPA})Pb_2I_6$	3D	377	464.42 mA/W	4.051×10^{12}	10	**This work**
KNb_3O_8	1D	254	30 A W^{-1}	5.9×10^{11}	5	[24]
$(C_8H_{11}FN)_2PbBr_4$	2D	254	288 mA W^{-1}	1.6×10^{11}	10	[25]
$(BDA)CdBr_4$	2D	254	2.452 μAW^{-1}		10	[26]
$NdNb_2O_7$	2D	260	62 AW^{-1}	6.7×10^{12}	3	[27]
$Cs_mSb_nCl_{m+3n}$	3D	266	39.5 μAW^{-1}		30	[28]
$(i\text{-BA})_2(MA)Pb_2Cl_7$	2D	266	67.8 $\mu A\ W^{-1}$	2.02×10^9	Self-powered	[29]

Materials	Dimensionality	Wavelength (nm)	Responsivity (R)	Detectivity (D*/Jones)	Condition (V)	Ref.
$Ca_2Nb_3O_{10}$	2D	280	14.94 A W^{-1}	8.7×10^{13}	3	[30]
$MAPbI_3$ nanoribbon arrays	1D	300	38.90mA W^{-1}	8.21×10^{11}	2	[31]
$(BA)_2Pb(Cl_{0.1}Br_{0.9})_4$	2D	340	3.19 mA W^{-1}	3.87×10^{11}	20	[32]
$(PEA)_2PbBr_4$	2D	360	1.67 A W^{-1}	2.11×10^{8}	18	[33]
$MAPbCl_3$/GaN	3D	360	86 mA W^{-1}	3.1×10^{11}	10	[34]
$CsSnX_3$ (X = Cl, Cl/Br, Br) QDs	3D	365		1.27×10^{11}	3	[35]
$MAPbCl_3$	3D	365	46.9 mA W^{-1}	1.2×10^{10}	15	[36]
$MAPbCl_3$	3D	365	3.37 A W^{-1}	9.97×10^{14}	30	[37]
$(BA)_2PbBr_4$	2D	377	16.9 mA W^{-1}	2.06×10^{12}	10	[38]
$MHyPbBr_3$	3D	377	198 mA W^{-1}	1.42×10^{13}	Self-powered	[39]
$(BPA)_2PbBr_4$	2D	377	0.1 mA W^{-1}	10^{7}	Self-powered	[40]
$(PA)_2PbBr_4$	2D	405	91.2 mA W^{-1}	6.02×10^{12}	10	[41]
$(BA)_2(MA)Pb_2Br_7$	2D	405	---	1.1×10^{9}	Self-powered	[42]
$BA_2CsPb_2Br_7$	2D	405	39.5 mA W^{-1}	1.2×10^{12}	Self-powered	[43]
$(i\text{-}PA)_2CsAgBiBr_7$	2D	405		---	10	[44]
$(AA)_2(EA)_2Pb_3Br_{10}$	2D	405		2.5×10^{9}	Self-powered	[45]
$(BA)_2(MA)_2Pb_3Br_{10}$	2D	405	---	3.6×10^{10}	Self-powered	[46]
$(BA)_2(FA)Pb_2Br_7$	2D	405	0.51 mA W^{-1}	1.47×10^{12}	Self-powered	[47]
$CsPbBr_3$ NWs	1D	442	5.49 A W^{-1}	---	0.4	[48]
$[CH(NH_2)_2][C(NH_2)_3]PbI_4$	2D	515		$\approx 10^{10}$	-3	[49]
$(PA)_2(FA)Pb_2I_7$	2D	520	---	1.73×10^{14}	10	[50]
$(FPEA)_2PbI_4$	2D	520		$\approx 10^{11}$	10	[51]
$MAPbI_3$ NWs	3D	530	4.94 A W^{-1}	2×10^{13}	1	[52]
$CsPbI_3$ NWs	3D	530	0.754 A W^{-1}	3.46×10^{10}	1	[53]
$MAPbBr_3$	3D	532	0.008 A W^{-1}	1.08×10^{10}	1.11	[54]
$iBAPbI_4$	2D	560		1.23×10^{10}	-5	[55]
$(EMA)_2(MA)Pb_2I_7$	2D	600	3.87 mA W^{-1}	2.92×10^{10}	9.5	[56]
$(PEA)_2(MA)_{n-1}Pb_nI_{3n+1}$	2D	633	89.8 A W^{-1}	1.58×10^{12}	5	[57]
$(iBA)_2(MA)Pb_2I_7$	2D	637		$\approx 10^{11}$	10	[58]
$MAPbICl_2/TiO_2$/Si	1D	800	870 mA W^{-1}	6×10^{12}	4	[59]
$(BDA)(EA)_2Pb_3Br_{10}$	2D	808		5.9×10^{8}	Self-powered	[60]
$PdSe_2$	2D	4600		6.7×10^{6}	Self-powered	[61]

Materials	Dimensio nality	Wavelength (nm)	Responsivity (R)	Detectivity (D*/Jones)	Condition (V)	Ref.
$(HDA)_2CsPb_2Br_7$	2D	405	0.21 mA W^{-1}	1.5×10^9	10	[62]

Reference

[1] C. C. Fan, B. D. Liang, C. D. Liu, C. Y. Chai, X. Bin Han and W. Zhang, Stable organic lead iodides with three-dimensional crystallographic and electronic structures showing high photoresponse, *Inorg. Chem. Front.*, 2022, **9**, 6404-6411.

[2] X. Li, Y. He, M. Kepenekian, P. Guo, W. Ke, J. Even, C. Katan, C. C. Stoumpos, R. D. Schaller and M. G. Kanatzidis, Three-Dimensional Lead Iodide Perovskitoid Hybrids with High X-ray Photoresponse, *J. Am. Chem. Soc.*, 2020, **142**, 6625-6637.

[3] C. C. Fan, C. D. Liu, B. D. Liang, T. Y. Ju, W. Wang, M. L. Jin, C. Y. Chai and W. Zhang, Chiral three-dimensional organic-inorganic lead iodide hybrid semiconductors, *Chem. Sci.*, 2024, **15**, 11374-11381.

[4] B. Bin Zhang, X. Liu, B. Xiao, A. Ben Hafsia, K. Gao, Y. Xu, J. Zhou and Y. Chen, High-Performance X-ray Detection Based on One-Dimensional Inorganic Halide Perovskite $CsPbI_3$, J. Phys. Chem, 2020, **11**, 432-437.

[5] J. Di, H. Li, J. Su, H. Yuan, Z. Lin, K. Zhao, J. Chang and Y. Hao, Reveal the Humidity Effect on the Phase Pure $CsPbBr_3$ Single Crystals Formation at Room Temperature and Its Application for Ultrahigh Sensitive X-Ray Detector, *Adv. Sci.*, 2022, **9**, 2103482.

[6] Q. Guan, S. You, Z. K. Zhu, R. Li, H. Ye, C. Zhang, H. Li, C. Ji, X. Liu and J. Luo, Three-Dimensional Polar Perovskites for Highly Sensitive Self-Driven X-Ray Detection, *Angew. Chem. Int. Ed.*, 2024, **63**, e202320180.

[7] Q. Guan, T. Zhu, Z. K. Zhu, H. Ye, S. You, P. Xu, J. Wu, X. Niu, C. Zhang, X. Liu and J. Luo, Unprecedented Chiral Three-dimensional Hybrid Organic-Inorganic Perovskitoids, *Angew. Chem. Int. Ed.*, 2023, **62**, e202307034.

[8] Y. Ma, W. Li, Y. Liu, W. Guo, H. Xu, S. Han, L. Tang, Q. Fan, J. Luo and Z. Sun, X-ray-Induced Pyroelectric Effect in a Perovskite Ferroelectric Drives Low Detection Limit Self-Powered Responses, *ACS Cent. Sci.*, 2023, **9**, 2350-2357.

[9] N. Li, Y. Li, S. Xie, J. Wu, N. Liu, Y. Yu, Q. Lin, Y. Liu, S. Yang, G. Lian, Y. Fang, D. Yang, Z. Chen and X. Tao, High-Performance and Self-Powered X-Ray Detectors Made of Smooth Perovskite Microcrystalline Films with 100 μm Grains, *Angew. Chem. Int. Ed.*, 2023, **62**, e202302435.

[10] J. Wu, L. Wang, A. Feng, S. Yang, N. Li, X. Jiang, N. Liu, S. Xie, X. Guo, Y. Fang, Z. Chen, D. Yang and X. Tao, Self-Powered $FA_{0.55}MA_{0.45}PbI_3$ Single-Crystal Perovskite X-Ray

Detectors with High Sensitivity, *Adv. Funct. Mater*, 2022, **32**, 2109149.

[11] S. You, P. Yu, J. Wu, Z. K. Zhu, Q. Guan, L. Li, C. Ji, X. Liu and J. Luo, Weak X-Ray to Visible Lights Detection Enabled by a 2D Multilayered Lead Iodide Perovskite with Iodine-Substituted Spacer, *Adv. Sci.*, 2023, **10**, 2301149.

[12] H. Li, J. Song, W. Pan, D. Xu, W. an Zhu, H. Wei and B. Yang, Sensitive and Stable 2D Perovskite Single-Crystal X-ray Detectors Enabled by a Supramolecular Anchor, *Adv. Mater.*, 2020, **32**, 2003790.

[13] Y. Shen, Y. Liu, H. Ye, Y. Zheng, Q. Wei, Y. Xia, Y. Chen, K. Zhao, W. Huang and S. Liu, Centimeter-Sized Single Crystal of Two-Dimensional Halide Perovskites Incorporating Straight-Chain Symmetric Diammonium Ion for X-Ray Detection, *Angew. Chem. Int. Ed.*, 2020, **59**, 14896-14902.

[14] W. Wei, Y. Zhang, Q. Xu, H. Wei, Y. Fang, Q. Wang, Y. Deng, T. Li, A. Gruverman, L. Cao and J. Huang, Monolithic integration of hybrid perovskite single crystals with heterogenous substrate for highly sensitive X-ray imaging, *Nat. Photonics*, 2017, **11**, 315-321.

[15] Y. He, L. Matei, H. J. Jung, K. M. McCall, M. Chen, C. C. Stoumpos, Z. Liu, J. A. Peters, D. Y. Chung, B. W. Wessels, M. R. Wasielewski, V. P. Dravid, A. Burger and M. G. Kanatzidis, High spectral resolution of gamma-rays at room temperature by perovskite $CsPbBr_3$ single crystals, *Nat. Commun.*, 2018, **9**, 1609.

[16] Y. Fan, Q. Chen, Z. Li, T. Zhu, J. Wu, S. You, S. Zhang, J. Luo and C. Ji, Realization of Passive X-Ray Detection with a Low Detection Limit in Dion-Jacobson Halide Hybrid Perovskite, *Small*, 2023, **19**, 202303814.

[17] C. Ma, L. Gao, Z. Xu, X. Li, X. Song, Y. Liu, T. Yang, H. Li, Y. Du, G. Zhao, X. Liu, M. G. Kanatzidis, S. F. Liu and K. Zhao, *Chemistry of Materials*, 2022, **34**, 1699-1709.

[18] S. Yakunin, D. N. Dirin, Y. Shynkarenko, V. Morad, I. Cherniukh, O. Nazarenko, D. Kreil, T. Nauser, M. V. Kovalenko, Centimeter-Sized 2D Perovskitoid Single Crystals for Efficient X-ray Photoresponsivity, *Nat. Photonics*, 2016, **10**, 585-589.

[19] Y. Zhang, Y. Liu, Z. Xu, H. Ye, Z. Yang, J. You, M. Liu, Y. He, M. G. Kanatzidis and S. (Frank) Liu, Nucleation-controlled growth of superior lead-free perovskite $Cs_3Bi_2I_9$ single-crystals for high-performance X-ray detection, *Nat. Commun.*, 2020, **11**, 2304.

[20] X. Dong, T. Chen, J. Liang, L. Wang, H. Wu, Z. Xu, J. Luo and L.-N. Li, Structure design of lead-free chiral-polar perovskites for sensitive self-powered X-ray detection, *Chin. J. Struct. Chem.*, 2024, **43**, 100256.

[21] X. Zheng, W. Zhao, P. Wang, H. Tan, M. I. Saidaminov, S. Tie, L. Chen, Y. Peng, J. Long and W. H. Zhang, Ultrasensitive and stable X-ray detection using zero-dimensional lead-

free perovskites, *J. Energy. Chem.*, 2020, **49**, 299-306.

[22] S. You, Z. K. Zhu, S. Dai, J. Wu, Q. Guan, T. Zhu, P. Yu, C. Chen, Q. Chen and J. Luo, Inch-Size Single Crystals of Lead-Free Chiral Perovskites with Bulk Photovoltaic Effect for Stable Self-Driven X-Ray Detection, *Adv. Funct. Mater*, 2023, **33**, 202303523.

[23] W. Li, D. Xin, S. Tie, J. Ren, S. Dong, L. Lei, X. Zheng, Y. Zhao and W. H. Zhang, Zero-Dimensional Lead-Free $FA_3Bi_2I_9$ Single Crystals for High-Performance X-ray Detection, *Phys. Chem. Lett*, 2021, **12**, 1778-1785.

[24] Y. Ping, H. Long, H. Liu, C. Chen, N. Zhang, H. Jing, J. Lu, Y. Zhao, Z. Yang, W. Li, F. Ma, X. Fang, Z. Wei and H. Xu, Polarization Sensitive Solar-Blind Ultraviolet Photodetectors Based on Ultrawide Bandgap KNb_3O_8 Nanobelt with Fringe-Like Atomic Lattice, *Adv. Funct. Mater*, 2022, **32**, 2111673.

[25] Y. Wang, B. Su, G. Lin, H. Lou, S. Wang, C. Y. Yue and X. Lei, Exploring the Ruddlesden-Popper layered organic-inorganic hybrid semiconducting perovskite for visible-blind ultraviolet photodetection, *CrystEngComm*, 2021, **24**, 2258-2263.

[26] Y. Wang, C. Ji, X. Liu, S. Han, J. Zhang, Z. Sun, A. Khan and J. Luo, (1,4-Butyldiammonium)$CdBr_4$: A layered organic-inorganic hybrid perovskite with a visible-blind ultraviolet photoelectric response, *Inorg. Chem. Front*, 2018, **5**, 2450-2455.

[27] Y. Zhang, J. Yao, Y. Teng, Z. Zhang, L. Wang, X. Wang, Y. Li, L. Kang, J. H. He and X. Fang, Two-dimensional perovskite $NdNb_2O_7$ for high-performance UV photodetectors by a general exfoliation and assembly strategy, *Nano Energ.*, 2023, **117**, 108915.

[28] W. Wang, S. Xu, Z. Lai, X. Feng, H. Qi, Q. Pan, Z. Yang, J. Kang, Y. Li, X. Shu, Z. Zhang, Y. Zhu, J. Bai, F. Hong, J. Qin, R. Xu, Y. He, F. Xu and L. Wang, Regulating the microscopic structure of solutions to synthesize centimeter-sized low-dimensional $Cs_mSb_nCl_{m+3n}$ perovskite single crystals for visible-blind ultraviolet photodetectors, *Inorg. Chem. Front*, 2023, **11**, 589-601.

[29] L. Lu, W. Weng, Y. Ma, Y. Liu, S. Han, X. Liu, H. Xu, W. Lin, Z. Sun and J. Luo, Anisotropy in a 2D Perovskite Ferroelectric Drives Self-Powered Polarization-Sensitive Photoresponse for Ultraviolet Solar-Blind Polarized-Light Detection, *Angew. Chem. Int. Ed.*, 2022, **61**, e202205030.

[30] Y. Zhang, S. Li, Z. Li, H. Liu, X. Liu, J. Chen and X. Fang, High-Performance Two-Dimensional Perovskite $Ca_2Nb_3O_{10}$ UV Photodetectors, *Nano Lett*, 2021, **21**, 382-388.

[31] S. Lim, M. Ha, Y. Lee and H. Ko, Large-Area, Solution-Processed, Hierarchical $MAPbI_3$ Nanoribbon Arrays for Self-Powered Flexible Photodetectors, *Adv. Opt. Mater.*, 2018, **6**, 1800615.

[32] Q. Wang, H. Wang, M. Sun, R. Xue, M. Ning, S. li, P. Chen and Z. Li, Two-dimensional hybrid perovskite crystals for highly sensitive and stable UV light detector, Opt. Mater., 2023, **145**, 114408.

[33] T. Guo, C. Tian, S. Zhao, Z. Chu, J. Ma, Y. Li, Z. Shi and G. Ran, Gravity-Guided Growth of Large-Area High-Quality Two-Dimensional Ruddlesden-Popper Perovskite Thin Films for Stable Ultraviolet Photodetectors, *Phys. Chem. C.*, 2021, **125**, 13909-13916.

[34] J. He, S. Jiang, L. Lu, W. Li, J. Zhang, W. Wei, Z. Guo, B. Hu, Z. Wan, Y. Yun, Y. Tian, K. Huang, M. Chen and C. Li, All-solution-processed perovskite/gallium nitride particles hybrid visible-blind ultraviolet photodetectors, *Nanotechnology*, 2023, **34**, 315202.

[35] Y. Wang, S. Bai, H. Liang, C. Li, J. Sun, X. Li, T. Tan, G. Yang and J. Wang, Cesium tin halide perovskite quantum dots for high-performance ultraviolet photodetectors, *J. Lumin*, 2023, **257**, 119700.

[36] G. Maculan, A. D. Sheikh, A. L. Abdelhady, M. I. Saidaminov, M. A. Haque, B. Murali, E. Alarousu, O. F. Mohammed, T. Wu and O. M. Bakr, $CH_3NH_3PbCl_3$ Single Crystals: Inverse Temperature Crystallization and Visible-Blind UV-Photodetector, *Phys. Chem. Lett*, 2015, **6**, 3781-3786.

[37] Z. Cheng, K. Liu, J. Yang, X. Chen, X. Xie, B. Li, Z. Zhang, L. Liu, C. Shan and D. Shen, High-Performance Planar-Type Ultraviolet Photodetector Based on High-Quality $CH_3NH_3PbCl_3$ Perovskite Single Crystals, *ACS Appl. Mater. Interfaces*, 2019, **11**, 34144-34150.

[38] L. Liang, X. Niu, X. Zhang, Z. Wang, J. Wu and J. Luo, Ultraviolet Photodetection with Low Detection Limit Using Inch-Sized Two-Dimensional Hybrid Perovskite Crystal, *Adv. Opt. Mater.*, 2022, **10**, 2201342.

[39] H. Li, Z. Wang, Q. Guan, C. Ji, R. Li, H. Ye, Z. Wu, C. Zhang and J. Luo, Polar Three-dimensional Organic-inorganic Hybrid Perovskite Realize Highly Sensitive Self-driven Ultraviolet Photodetection, *Angew. Chem. Int. Ed.*, 2025, **64**, e202500765.

[40] C. Ji, D. Dey, Y. Peng, X. Liu, L. Li and J. Luo, Ferroelectricity-Driven Self-Powered Ultraviolet Photodetection with Strong Polarization Sensitivity in a Two-Dimensional Halide Hybrid Perovskite, *Angew. Chem. Int. Ed.*, 2020, **59**, 18933-18937.

[41] C. Zhang, H. Xiao, Q. Guan, T. Zhu, L. Liang, R. Li, H. Ye, X. Niu and J. Luo, Centimeter-size single crystals of 2D hybrid perovskites for shortwave light photodetection with a low detection limit, *J. Mater. Chem. C*, 2023, **11**, 5116-5122.

[42] L. Li, X. Liu, Y. Li, Z. Xu, Z. Wu, S. Han, K. Tao, M. Hong, J. Luo and Z. Sun, Two-Dimensional Hybrid Perovskite-Type Ferroelectric for Highly Polarization-Sensitive

Shortwave Photodetection, *J. Am. Chem. Soc.*, 2019, **141**, 2623-2629.
[43] J. Wang, Y. Liu, S. Han, Y. Ma, Y. Li, Z. Xu, J. Luo, M. Hong and Z. Sun, Ultrasensitive polarized-light photodetectors based on 2D hybrid perovskite ferroelectric crystals with a low detection limit, *Sci. Bull.*, 2021, **66**, 158-163.
[44] Y. Li, T. Yang, Z. Xu, X. Liu, X. Huang, S. Han, Y. Liu, M. Li, J. Luo and Z. Sun, Dimensional Reduction of $Cs_2AgBiBr_6$: A 2D Hybrid Double Perovskite with Strong Polarization Sensitivity, *Angew. Chem. Int. Ed.*, 2020, **132**, 3457-3461.
[45] Y. Peng, X. Liu, Z. Sun, C. Ji, L. Li, Z. Wu, S. Wang, Y. Yao, M. Hong and J. Luo, Exploiting the Bulk Photovoltaic Effect in a 2D Trilayered Hybrid Ferroelectric for Highly Sensitive Polarized Light Detection, *Angew. Chem. Int. Ed.*, 2020, **132**, 3961-3965.
[46] L. Li, Z. Sun, P. Wang, W. Hu, S. Wang, C. Ji, M. Hong and J. Luo, Tailored Engineering of an Unusual $(C_4H_9NH_3)_2(CH_3NH_3)_2Pb_3Br_{10}$ Two-Dimensional Multilayered Perovskite Ferroelectric for a High-Performance Photodetector, *Angew. Chem. Int. Ed.*, 2017, **129**, 12318-12322.
[47] Z. Xu, X. Dong, L. Wang, H. Wu, Y. Liu, J. Luo, M. Hong and L. Li, Precisely Tailoring a $FAPbI_3$-Derived Ferroelectric for Sensitive Self-Driven Broad-Spectrum Polarized Photodetection, *J. Am. Chem. Soc.,* 2023, **145**, 1524-1529.
[48] S. Pan, H. Zou, A. C. Wang, Z. Wang, J. Yu, C. Lan, Q. Liu, Z. L. Wang, T. Lian, J. Peng and Z. Lin, Rapid Capillary-Assisted Solution Printing of Perovskite Nanowire Arrays Enables Scalable Production of Photodetectors, *Angew. Chem. Int. Ed.*, 2020, **59**, 14942-14949.
[49] C. Fang, M. Xu, J. Ma, J. Wang, L. Jin, M. Xu and D. Li, Large Optical Anisotropy in Two-Dimensional Perovskite $[CH(NH_2)_2][C(NH_2)_3]PbI_4$ with Corrugated Inorganic Layers, *Nano Lett*, 2020, **20**, 2339-2347.
[50] S. Han, Y. Yao, X. Liu, B. Li, C. Ji, Z. Sun, M. Hong and J. Luo, Highly Oriented Thin Films of 2D Ruddlesden-Popper Hybrid Perovskite toward Superfast Response Photodetectors, *Small*, 2019, **15**, 1901194.
[51] M. Li, S. Han, B. Teng, Y. Li, Y. Liu, X. Liu, J. Luo, M. Hong and Z. Sun, Minute-Scale Rapid Crystallization of a Highly Dichroic 2D Hybrid Perovskite Crystal toward Efficient Polarization-Sensitive Photodetector, *Adv. Opt. Mater.*, 2020, **8**, 202000149.
[52] L. Gao, K. Zeng, J. Guo, C. Ge, J. Du, Y. Zhao, C. Chen, H. Deng, Y. He, H. Song, G. Niu and J. Tang, Passivated Single-Crystalline $CH_3NH_3PbI_3$ Nanowire Photodetector with High Detectivity and Polarization Sensitivity, *Nano Lett*, 2016, 16, 7446-7454.
[53] Y. Zhou, J. Luo, Y. Zhao, C. Ge, C. Wang, L. Gao, C. Zhang, M. Hu, G. Niu and J. Tang, Flexible Linearly Polarized Photodetectors Based on All-Inorganic Perovskite $CsPbI_3$

Nanowires, *Adv. Opt. Mater.*, 2018, **6**, 1800679.
[54] J. Zhang, J. Zhao, Y. Zhou, Y. Wang, K. S. Blankenagel, X. Wang, M. Tabassum and L. Su, Polarization-Sensitive Photodetector Using Patterned Perovskite Single-Crystalline Thin Films, *Adv. Opt. Mater.*, 2021, **9**, 2100524.
[55] L. Li, L. Jin, Y. Zhou, J. Li, J. Ma, S. Wang, W. Li and D. Li, Filterless Polarization-Sensitive 2D Perovskite Narrowband Photodetectors, *Adv. Opt. Mater.,* 2019, **7**, 1900988.
[56] S. Han, P. Wang, J. Zhang, X. Liu, Z. Sun, X. Huang, L. Li, C. Ji, W. Zhang, B. Teng, W. Hu, M. Hong and J. Luo, Exploring a Polar Two-dimensional Multi-layered Hybrid Perovskite of $(C_5H_{11}NH_3)_2(CH_3NH_3)Pb_2I_7$ for Ultrafast-Responding Photodetection, *Laser & Photonics Rev.*, 2018, **12**, 1800060.
[57] D. Liu, Q. Wei, L. Zhuang, M. Liu, L. Zeng, H. Ren, M. Li and S. P. Lau, Nanoimprinted Quasi-2D Perovskites toward High-Performance Polarization-Sensitive Photodetectors, *Adv. Opt. Mater.*, 2024, **12**, 2302411.
[58] Y. Liu, Z. Wu, X. Liu, S. Han, Y. Li, T. Yang, Y. Ma, M. Hong, J. Luo and Z. Sun, Intrinsic Strong Linear Dichroism of Multilayered 2D Hybrid Perovskite Crystals toward Highly Polarized-Sensitive Photodetection, *Adv. Opt. Mater.*, 2019, **7**, 1901049.
[59] F. Cao, Q. Liao, K. Deng, L. Chen, L. Li and Y. Zhang, Novel perovskite/TiO_2/Si trilayer heterojunctions for high-performance self-powered ultraviolet-visible-near infrared (UV-Vis-NIR) photodetectors, *Nano Res.*, 2018, **11**, 1722-1730.
[60] H. Ye, Y. Peng, X. Shang, L. Li, Y. Yao, X. Zhang, T. Zhu, X. Liu, X. Chen and J. Luo, Self-Powered Visible-Infrared Polarization Photodetection Driven by Ferroelectric Photovoltaic Effect in a Dion–Jacobson Hybrid Perovskite, *Adv. Funct. Mater*, 2022, **32**, 2200223.
[61] M. Dai, C. Wang, M. Ye, S. Zhu, S. Han, F. Sun, W. Chen, Y. Jin, Y. Chua and Q. J. Wang, High-Performance, Polarization-Sensitive, Long-Wave Infrared Photodetection via Photothermoelectric Effect with Asymmetric van der Waals Contacts, *ACS NANO*, 2022, **16**, 295-305.
[62] T. Yang, Y. Li, S. Han, Z. Xu, Y. Liu, X. Zhang, X. Liu, B. Teng, J. Luo and Z. Sun, Highly-Anisotropic Dion–Jacobson Hybrid Perovskite by Tailoring Diamine into $CsPbBr_3$ for Polarization-Sensitive Photodetection, *Small*, 2020, **16**, 1907020.